

RESEARCH ARTICLE

Optically modulated dual-mode memristor arrays based on core-shell CsPbBr₃@graphdiyne nanocrystals for fully memristive neuromorphic computing hardware

Fu-Dong Wang¹ | Mei-Xi Yu¹ | Xu-Dong Chen^{1,2}  | Jiaqiang Li³ | Zhi-Cheng Zhang² | Yuan Li¹ | Guo-Xin Zhang¹ | Ke Shi¹ | Lei Shi¹ | Min Zhang¹ | Tong-Bu Lu¹ | Jin Zhang³

¹MOE International Joint Laboratory of Materials Microstructure, Institute for New Energy Materials and Low Carbon Technologies, School of Materials Science and Engineering, Tianjin University of Technology, Tianjin, China

²The Key Laboratory of Weak Light Nonlinear Photonics, Ministry of Education, School of Physics, Nankai University, Tianjin, China

³Center for Nanochemistry, Beijing Science and Engineering Center for Nanocarbons, Beijing National Laboratory for Molecular Sciences, College of Chemistry and Molecular Engineering, Peking University, Beijing, China

Correspondence

Dr. Xu-Dong Chen, Min Zhang, and Tong-Bu Lu, MOE International Joint Laboratory of Materials Microstructure, Institute for New Energy Materials and Low Carbon Technologies, School of Materials Science and Engineering, Tianjin University of Technology, Tianjin 300384, China.
Email: chenxd@email.tjut.edu.cn; zm2016@email.tjut.edu.cn and lutongbu@tjut.edu.cn

Jin Zhang Prof., Center for Nanochemistry, Beijing Science and Engineering Center for Nanocarbons, Beijing National Laboratory for Molecular Sciences, College of Chemistry and Molecular Engineering, Peking University, Beijing 100871, China.
Email: jinzhang@pku.edu.cn

Funding information

Natural Science Foundation of Tianjin City, Grant/Award Number: 19JCYBJC17300; National Natural Science Foundation of China, Grant/Award Numbers: 21790052, 51802220

Abstract

Artificial synapses and neurons are crucial milestones for neuromorphic computing hardware, and memristors with resistive and threshold switching characteristics are regarded as the most promising candidates for the construction of hardware neural networks. However, most of the memristors can only operate in one mode, that is, resistive switching or threshold switching, and distinct memristors are required to construct fully memristive neuromorphic computing hardware, making it more complex for the fabrication and integration of the hardware. Herein, we propose a flexible dual-mode memristor array based on core-shell CsPbBr₃@graphdiyne nanocrystals, which features a 100% transition yield, small cycle-to-cycle and device-to-device variability, excellent flexibility, and environmental stability. Based on this dual-mode memristor, homo-material-based fully memristive neuromorphic computing hardware—a power-free artificial nociceptive signal processing system and a spiking neural network—are constructed for the first time. Our dual-mode memristors greatly simplify the fabrication and integration of fully memristive neuromorphic systems.

KEYWORDS

dual-mode memristors, metal halide perovskites, neuromorphic computing, nociceptors, spiking neural networks

Fu-Dong Wang and Mei-Xi Yu contributed equally to this work.

This is an open access article under the terms of the [Creative Commons Attribution](https://creativecommons.org/licenses/by/4.0/) License, which permits use, distribution and reproduction in any medium, provided the original work is properly cited.

© 2022 The Authors. *SmartMat* published by Tianjin University and John Wiley & Sons Australia, Ltd.

1 | INTRODUCTION

In the era of artificial intelligence (AI) and internet of things (IoT), massive sensory data including images, sound, smell, and injury are perceived from the external environment, imposing critical requirements on the processing speed and energy efficiency for the data-centric tasks.^{1–3} Although great efforts have been made to improve the computing capability and efficiency of von Neumann computers, the constant data shuttling between the physically separated processing and memory units would inevitably consume huge energy and induce computing latency.^{4–9} Alternatively, the human brain-inspired neuromorphic computing based on artificial neural networks (ANNs) has demonstrated its great advantages in data-intensive applications such as AI and machine learning. For the hardware implementation of ANNs, two key elements, that is, artificial synapses and neurons, must be developed to emulate the physiological activities of biological synapses and neurons, respectively. In recent years, various neuromorphic devices have been proposed,^{10–13} in which two-terminal memristors are regarded as the most promising candidates due to their simple architecture, high integration density, high operation speed, low energy consumption, and analog behaviors.^{1,2,7,8,14–17} Especially, the recently proposed diffusive memristors featuring volatile threshold switching (TS) behaviors have demonstrated their potential in leaky integrate-and-fire (LIF) neurons,^{5,7,18,19} paving a simple way to emulate neural functions. Given the high energy efficiency and integration density of memristor crossbar arrays in comparison with their complementary metal-oxide-semiconductor (CMOS) counterparts,^{20,21} fully memristive neuromorphic computing hardware consisting of nonvolatile drift memristors and volatile diffusive memristors is highly desirable.

Thus far, the drift and diffusive memristors used in the reported neuromorphic computing hardware are different.^{5,18,19,22} For example, drift memristors with a stack of Pd/HfO₂/Ta were used as the artificial synapses, whereas Pt/SiO_x:Ag/Pt diffusive memristors served as the neurons.¹⁸ The distinct components and structures of the drift and diffusive memristors inevitably make the fabrication and integration of the hardware ANNs more complex. Alternatively, a memristor that can achieve both nonvolatile resistive switching (RS) and volatile TS behaviors will significantly simplify the fabrication process. Thus far, only a few of the reported memristors can realize the transition between RS and TS modes, mainly by varying electrical forming conditions and compliance current (I_{CC}), or optical doping.^{7,23,24} However, these devices still suffer great challenges in application of fully memristive neuromorphic computing

hardware. For instance, the memristive characteristic of the dual-mode memristor controlled by electrical forming conditions is determined once the forming process finishes, and the transition between RS and TS modes is not available anymore.²⁴ On the other hand, for the I_{CC} -controlled dual-mode memristor, the I_{CC} used to control the RS/TS transition varies for different devices due to the device-to-device variation (DDV), and every device requires a separate I_{CC} value, which is challenging for large-scale device arrays. Especially, these studies mainly focus on the performance of a single device, ignoring the DDV and the yield of the transition between RS and TS modes, which are crucial for system-level applications.

Metal halide perovskites (MHPs) are emerging materials for neuromorphic applications due to their extraordinary optoelectronic properties and ionic-electronic mixed conduction characteristics.^{5,25–27} Various neuromorphic devices including photonic synapses, two-terminal drift and diffusive memristors, and three-terminal synaptic transistors have been developed based on MHPs.^{5,25,26,28–30} Given the intrinsic ionic nature of MHPs, they are very sensitive to ambient environment, and exposing to water, oxygen or even continuous light irradiation can severely degrade the performance of MHP-based devices.^{31,32} Thus improving the environmental stability of MHPs is crucial for practical applications, but it has rarely been considered in the reported neuromorphic devices.

In this study, we construct a flexible dual-mode memristor array based on core-shell CsPbBr₃@graphdiyne (GDY) nanocrystals with optically modulated threshold and resistive switching behaviors. In the dark condition, the memristor operates in the nonvolatile RS mode, which can emulate the synaptic functions. While the memristor is irradiated, the well-designed band structures of CsPbBr₃ and GDY facilitate the separation and transfer of photo-generated electron-hole pairs, leading to the dissolution of Ag conductive filaments (CFs). As a result, the memristor demonstrates the volatile TS behavior, enabling the construction of artificial neurons. The yield of the transition between RS and TS modes is 100%. Here a power-free artificial nociceptive signal processing system (ANSPTS) and a spiking neural network (SNN) have been developed, in which the nociceptors, spiking neurons and artificial synapses are all implemented by our CsPbBr₃@GDY-based memristors. This is the first demonstration of fully memristive neuromorphic computing hardware at the system level comprising only one kind of memristors. Moreover, the encapsulation of the shell GDY layer can well protect the inner CsPbBr₃ from damage in humid and oxygen environment, significantly improving the environmental stability of the memristor.

2 | RESULTS AND DISCUSSION

2.1 | Core-shell CsPbBr₃@GDY nanocrystals

Figure 1A illustrates the structure of the core-shell CsPbBr₃@GDY nanocrystal prepared via a two-step synthetic approach as described in Supporting

Information Note S1. Briefly, pristine inorganic perovskite CsPbBr₃ quantum dots (QDs) were first synthesized via a solution-phase strategy (Figures 1C and S1). Then GDY was in-situ synthesized on the surface of CsPbBr₃ QDs via a microwave-assisted strategy,³³ forming core-shell CsPbBr₃@GDY nanocrystals. The high-resolution transmission electron microscopy (HRTEM) image as depicted in Figure 1B

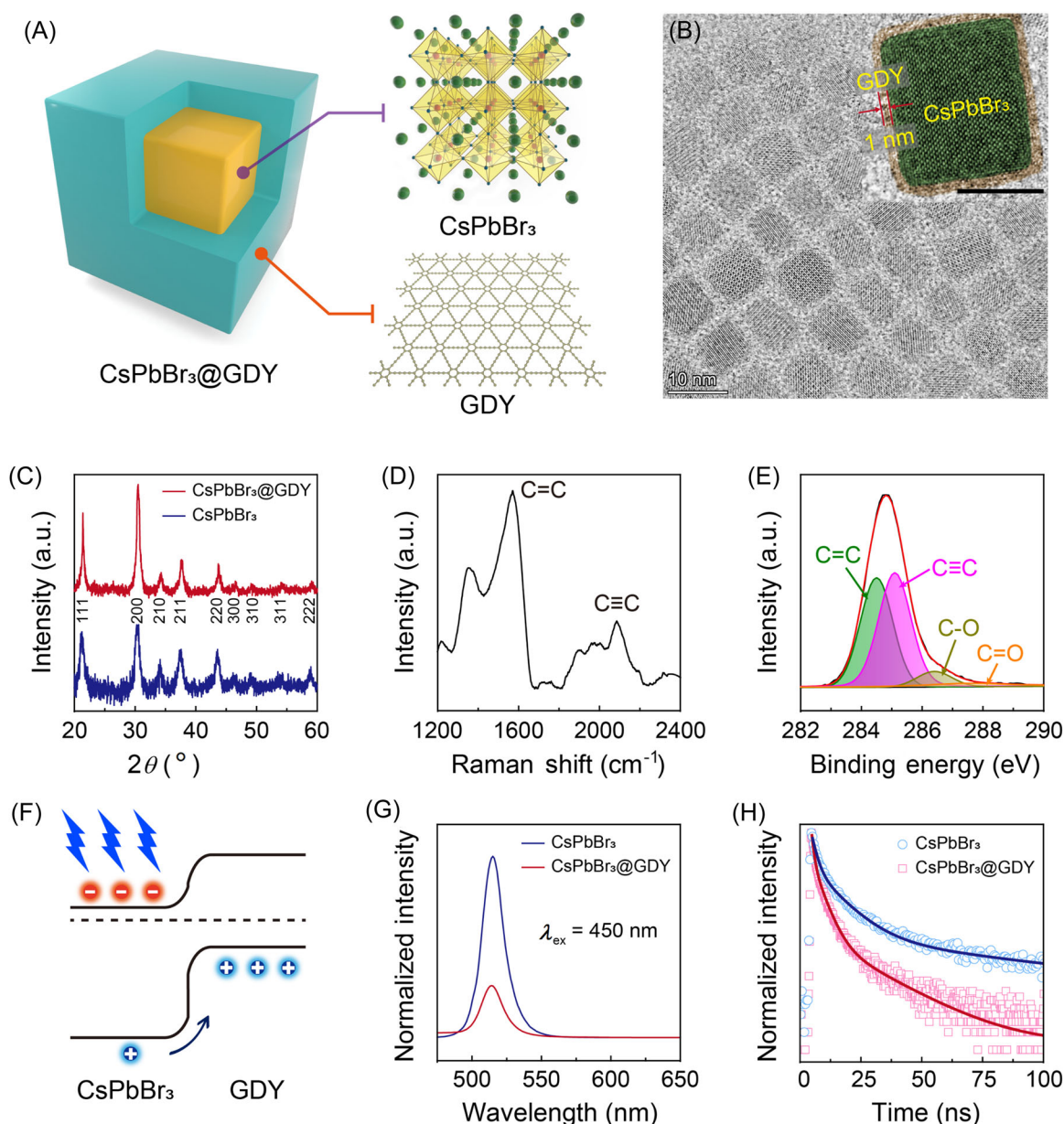


FIGURE 1 Characterization of the core-shell CsPbBr₃@GDY nanocrystals. (A) Schematic of the core-shell CsPbBr₃@GDY nanocrystals. Cubic CsPbBr₃ QDs (core) are wrapped tightly by GDY layer (shell). (B) TEM image of the core-shell CsPbBr₃@GDY nanocrystals. Inset: false-colored HRTEM image of the core-shell CsPbBr₃@GDY nanocrystal. Scale bars, 10 nm. (C) XRD patterns of the CsPbBr₃ QDs before (blue) and after (red) the synthesis of the shell GDY layer. (D) Raman spectrum of the CsPbBr₃@GDY nanocrystals. (E) C 1s peak of the XPS spectrum for the CsPbBr₃@GDY nanocrystals. (F) Band diagram of the CsPbBr₃/GDY heterojunction under equilibrium. (G) Steady-state and (H) transient PL spectra of the core-shell CsPbBr₃@GDY nanocrystals. $\lambda_{\text{ex}} = 450$ nm. GDY, graphdiyne; HRTEM, high-resolution transmission electron microscopy; QDs, quantum dots.

demonstrates the homogeneous distribution of the cubic CsPbBr₃@GDY nanocrystals with average size of 9.5 nm (Figure S2). The CsPbBr₃ QDs were wrapped tightly by the GDY layer with a thickness of approximately 1 nm (3 L, inset of Figure 1B). Figure 1D,E present the Raman and X-ray photoelectron spectroscopy (XPS) spectra of the as-prepared CsPbBr₃@GDY nanocrystals, where the Raman bands at 1571 and 2086 cm⁻¹, and the C 1s peak demonstrate the successful synthesis of GDY on CsPbBr₃ QDs.^{34,35}

To investigate the charge transfer between the core CsPbBr₃ and shell GDY layer, the energy bands of the CsPbBr₃ QDs and GDY were measured. The band gaps of CsPbBr₃ and GDY can be determined via the UV-vis spectra (Figure S3), which are 2.33 eV and 1.65 eV, respectively. According to the ultraviolet photoelectron spectroscopy (UPS) and Kelvin probe force microscopy (KPFM) measurements (Figures S4 and S5), the Fermi levels and valence bands of CsPbBr₃ and GDY are located at 4.15/6.25 eV (CsPbBr₃) and 5.03/5.51 eV (GDY), respectively. The work function mismatch between CsPbBr₃ and GDY results in an upward band bending at the CsPbBr₃/GDY interface (Figures 1F and S6). Under light illumination, the electron-hole pairs are mainly generated in the core CsPbBr₃ QDs owing to their significant photoresponse. Driven by the built-in electric field between CsPbBr₃ and GDY, the photogenerated holes would transfer to the shell GDY layer, while leaving electrons trapped in the core CsPbBr₃. The charge transfer between CsPbBr₃ and GDY can be demonstrated by the steady-state photoluminescence (PL) spectra and transient PL spectra. As shown in Figures 1G and S7, the PL intensity of CsPbBr₃ QDs is significantly quenched while coating GDY layer, indicating effective exciton splitting.^{26,36} The time-resolved PL decay traces of CsPbBr₃ and core-shell CsPbBr₃@GDY nanocrystals as present in Figure 1H can be fitted with a three-exponential function. Due to the fast exciton separation at the CsPbBr₃/GDY interface, the average lifetime of CsPbBr₃@GDY is calculated as 5.1 ns, which is noticeably shorter than that of pristine CsPbBr₃ (23 ns).^{26,36}

2.2 | Core-shell CsPbBr₃@GDY-based flexible memristor array

Based on the fabricated core-shell CsPbBr₃@GDY nanocrystals, a memristor array with a vertical crossbar structure (Ag/PMMA/CsPbBr₃@GDY/PMMA/indium tin oxide (ITO)) was constructed on a flexible poly(ethylene terephthalate) (PET) substrate, as illustrated in Figure 2A. Here ITO and active metal Ag are selected as the bottom

and top bar electrodes, respectively, while a close-packed CsPbBr₃@GDY layer sandwiched between two PMMA layers acts as the active layer. Note that the PMMA layers are used as the charge blocking layers for higher on/off ratio and better device stability (Figure S8).^{26,29} The cross-section TEM image as shown in Figure 2B clearly reveals a dense CsPbBr₃@GDY layer with a thickness of approximately 50 nm. To evaluate the quality of the as-prepared CsPbBr₃@GDY layer, atomic force microscopy (AFM) morphology measurement was performed, exhibiting a smooth surface with roughness of 0.21 nm (Figure S9).

The typical current-voltage (*I-V*) characterization of the core-shell CsPbBr₃@GDY-based memristor under dark condition was first investigated. As shown in Figure 2C, the device presents a repeatable bipolar RS characteristic with a relatively small cycle-to-cycle variability (CCV). During the positive voltage sweeping (0 V → 1 V → 0 V), the device switches from its high-resistance state (HRS) to low-resistance state (LRS) at around 0.65 V (SET) with an on/off ratio of 10⁵, and it returns to HRS at -0.76 V (RESET) in reverse voltage sweeping. The conduction of the device obeys the space-charge-limited current (SCLC) model (Figure S10).^{7,26} Figures S11 and 2D demonstrate the long-term retention characteristics (>10⁵ s) and robust endurance (10⁴ cycles) of the device. Given the perovskite QDs are quite unstable in humid environment, here the stability of the device in atmospheric environment with humidity of 80% and temperature of 50°C was investigated. As shown in Figure 2E, A typical RS behavior can still be observed even after 60 days, demonstrating its high stability in humid environment. In contrast, the memristor based on bare CsPbBr₃ QDs without GDY wrapping exhibits a relatively poor stability in humid environment (Figure S12). Thus we can conclude that the package of GDY can prevent the damage of water and oxygen to CsPbBr₃ QDs, significantly improving the stability of the device in humid environment. The impact of the CsPbBr₃@GDY layer thickness on the device performance was also investigated. As depicted in Figure S13, the RS behavior of the device with a thinner CsPbBr₃@GDY layer is unstable, whereas relatively larger V_{SET} and V_{RESET} are required for the device with a thicker CsPbBr₃@GDY layer. Thus the device fabricated by the CsPbBr₃@GDY with a thickness of 50 nm was used in the following electrical and optoelectronic measurement.

As depicted in Figure 2F, the I_{CC} has a significant influence on the performance of memristor, in which decreased V_{SET} and V_{RESET} are observed with the decrease of I_{CC} . As illustrated in Figure S14, a thicker Ag CF is formed under a higher I_{CC} , which requires more energy and thus a larger V_{RESET} for the RESET process. In turn, a

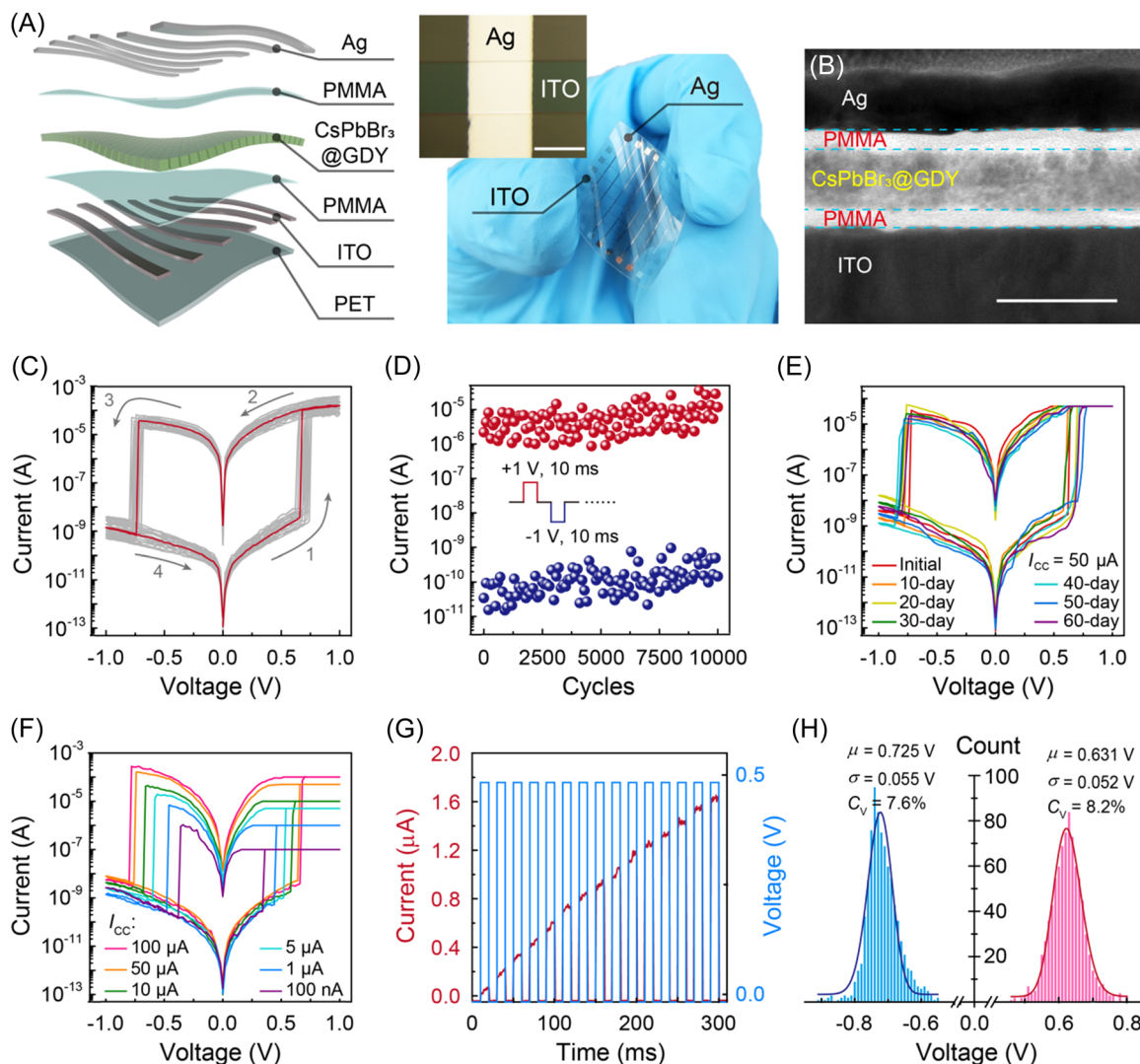


FIGURE 2 RS characteristics of the CsPbBr₃@GDY-based memristors. (A) Schematic (left) and photograph (right) of the memristor array fabricated on flexible PET substrate. Inset: optical microscopy (OM) image of a memristor crossbar structure. Scale bar, 100 μm . (B) Cross-section TEM image of the ITO/PMMA/CsPbBr₃@GDY/PMMA/Ag stacks. Scale bar, 100 nm. (C) Representative I - V curves measured from one single memristor. (D) Endurance test of the memristor for over 10^4 cycles. The inset illustrates the applied periodic pulse sequence, which consists of +1 V/10 ms SET pulse followed by a -1 V/10 ms RESET pulse. The currents of the memristor at HRS (blue) and LRS (red) were measured for every 100 cycles by a 0.1 V read pulse. (E) I - V characteristics of the memristor exposed to atmospheric environment with humidity of 80% and temperature of 50°C. I_{CC} was set as 50 μA . (F) I - V characteristics of the memristor at six different I_{CC} . (G) Analog transition of the memristor triggered by pulsed voltage sequence (0.5 V, 10 ms). (H) Statistical distribution of the SET (pink) and RESET (blue) voltages of 61 memristors using 50 μA current compliance. GDY, graphdiyne; HRS, high-resistance state; LRS, low-resistance state; PET, poly(ethylene terephthalate).

thicker ruptured CF requires a larger electric field to repair it during the SET process. That is, for a larger I_{CC} which induce thicker CFs, a larger V_{SET} is required to repair the ruptured CFs. Analog transition between different conductance states can be achieved by applying sequences of pulsed voltage stresses (Figure 2G), and over 16 stable intermediate-conductance states in range of 0.1–16 μS have been demonstrated (Figure S15). These features enable the use of CsPbBr₃@GDY-based memristor arrays for neuromorphic applications.

The crossbar architecture of memristor facilitates the fabrication of large-scale device arrays. As shown in Figure S16, an 8×8 device array was constructed to evaluate the yield and DDV of the CsPbBr₃@GDY-based memristors. In total, 61 of these devices feature RS behaviors (Figure S17), which indicates a quite high yield over 95%. Figure S18 depicts the statistical analysis of over 1000 I - V curves collected from these 61 devices. The CCV and DDV of the V_{SET} and V_{RESET} can be evaluated by the coefficient of variation (C_V) as

$C_V = \sigma/\mu$, where σ and μ are the standard deviation and the mean value, respectively.³⁷ For $I_{CC} = 50 \mu\text{A}$, the minimum CCVs of the V_{SET} and V_{RESET} obtained from a single device are calculated as 7.0% and 6.5%, respectively, while their DDVs collected from all 61 devices are 8.2% and 7.6%, respectively (Figure 2H). Figure S19 presents the cumulative probability of the conductance G_{HRS} and G_{LRS} obtained from 1000 cycles of 61 devices, and the median of the current window is over 10^4 , enabling reliable state distinction.

2.3 | Optically modulated transition between RS and TS modes

The transition of the $\text{CsPbBr}_3@\text{GDY}$ -based memristor between RS and TS modes can be achieved by light illumination. Figure 3A depicts the I - V characteristics of the devices with and without light illumination. Under light illumination (405 nm, $100 \mu\text{W}/\text{cm}^2$), the device spontaneously relaxes back to its initial HRS at around 0.1 V, demonstrating a volatile TS characteristic, which is

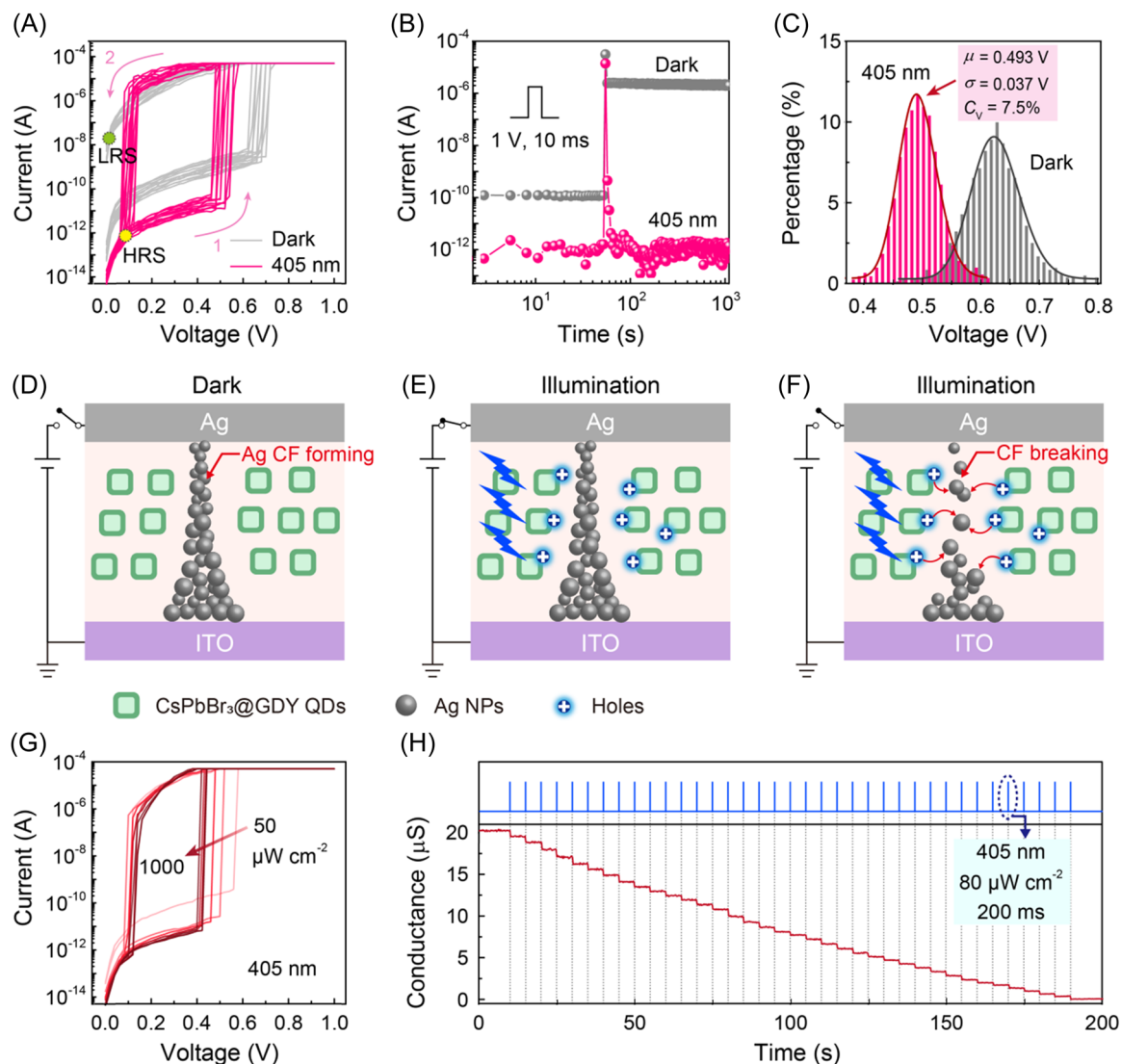


FIGURE 3 Optically modulated TS characteristics of the $\text{CsPbBr}_3@\text{GDY}$ -based memristors. (A) I - V curves of the memristor in the dark (gray curves) and under a 405 nm light illumination (pink curves), respectively. (B) Responses of the memristor to a 1 V/10 ms pulsed voltage in the dark (gray curve) and under a 405 nm light illumination (pink curve), respectively. The read voltage was fixed as 0.1 V. (C) Statistical distribution of the SET voltages of 61 memristors in the dark (gray) and under light illumination (pink), respectively. (D-F) Schematic of Ag CFs formation (D) in the dark and (E) under light illumination, and (F) photo-induced rupture of Ag CFs. (G) I - V characteristics of the memristor under a 405 nm light illumination with intensity ranging from 50 to $1000 \mu\text{W}/\text{cm}^2$. (H) Response of the memristor triggered by successive optical pulses (405 nm, $80 \mu\text{W}/\text{cm}^2$, width 200 ms). $V_{\text{read}} = 0.1$ V. GDY, graphdiyne; TS, threshold switching.

in contrast to the nonvolatile RS behavior without illumination. The transition of the volatility can be further verified by the transient response of the device triggered by a voltage pulse (1 V, 10 ms). As shown in Figure 3B, triggered by the programming pulse, the device switches to LRS and retains in LRS for over 10^3 s in the dark condition, whereas it immediately relaxes back to its initial HRS after pulse under light illumination. Noteworthily, this light-induced transition between RS and TS modes has been demonstrated in all the 61 memristors (Figure S20), indicating a 100% transition yield. Figures 3C and S21 statistically analyze the SET voltages (DDV 7.5%) and off currents of these devices under light illumination, which are obviously decreased in comparison with those of the devices in the dark condition. Compared with previously reported dual-mode memristors, the high transition yield and small DDV of our memristor make it more suitable for fully memristive neuromorphic applications. In fact, this study made the first effort to construct fully memristive neuromorphic computing hardware based on dual-mode memristors, which will be demonstrated below.

The transition of the memristor from RS mode to TS mode can be explained as following. Since the migration of Br^- in our core-shell $\text{CsPbBr}_3@$ GDY-based memristor is significantly suppressed by the shell GDY layer, the migration of Ag^+ and formation of Ag CFs driven by a positive voltage play a key role for the switching of the device from HRS to LRS.²⁹ These Ag CFs are stable in the dark condition, resulting in a nonvolatile RS characteristic (Figure 3D). In contrast, while the device is illuminated by a 405 nm light, photogenerated holes are accumulated at the shell GDY layer (Figure 3E). These holes can easily transfer to neighboring Ag CFs, and Ag tends to be oxidized to Ag^+ by accepting a hole (losing an electron).⁷ As a result, the Ag CFs are dissolved under light illumination after removing external voltage (Figure 3F), and the device switches from LRS to HRS spontaneously, demonstrating a volatile TS behavior.

As mentioned above, the photogenerated holes can oxidize the Ag to Ag^+ , which makes against the formation of Ag CFs. However, here a decreased V_{SET} was observed under illumination, which implies the existence of a competitive mechanism facilitating the formation of Ag CFs. As demonstrated in Figures S22 and S23, a large number of holes accumulated near the surface of $\text{CsPbBr}_3@$ GDY film under illumination, which induces a locally enhanced electrostatic field that can drive the movement of Ag^+ and thus facilitate the formation of Ag CFs, resulting in a decreased V_{SET} under illumination.⁷ The negative photoconductivity (NPC) phenomenon of the device in HRS can be explained by the decrease of charge filling levels in Ag-nanoparticle traps (Figure S24).^{7,38} The

photogenerated holes accumulated in the GDY layer recombine with the captured electrons in Ag nanoparticles. Since the conduction of the memristor at HRS obeys the SCLC model (Figure S10), the decrease of filling level in traps will lead to the decrease of conductance. This phenomenon can also be demonstrated by the Arrhenius behaviors and $I-t$ curves of the memristor at HRS in the dark and illumination conditions (Figures S25 and S26). In contrast, the bare CsPbBr_3 -based memristor exhibits a positive photoresponse, and it still remains RS characteristics even under light illumination (Figure S27), which indicates that the shell GDY layer is essential for the light-induced transition from RS to TS mode.

The light-intensity-dependent and wavelength-dependent characteristics of the optically modulated TS behaviors were investigated. Figure 3G depicts the $I-V$ curves of the memristor illuminated by a 405 nm light with different intensities. With the increase of irradiance intensity, the SET voltage and off current of the device exhibit an obvious decrease at beginning and finally tend to saturation (Figure S28). The wavelength-dependent $I-V$ characteristics of the device are shown in Figure S29. Obviously, the transition from RS to TS mode is closely related to the irradiation wavelength. Triggered by shorter wavelengths (e.g., 405 nm and 450 nm), the device operates in TS mode, while it still remains RS behavior under longer irradiation wavelengths (e.g., 532 nm and 633 nm).

Figure S30 depicts the response of the memristor at LRS to an optical pulse, in which the conductance of the device decreased to a lower level after the pulse. This is because that the conductive Ag CF is partially dissolved by the holes generated by neighboring $\text{CsPbBr}_3@$ GDY nanocrystals. By applying optical pulses with suitable intensity and duration, the conductance states can be continuously modulated. As depicted in Figure 3H, over 38 distinct conductive states have been obtained by applying successive light pulses. These conductance states feature excellent retention characteristics (Figure S31), demonstrating its potential for multibit storage and analog computation.^{35,39}

2.4 | Power-free artificial nociceptive signal processing system for robotics

Nociceptors are critical and special receptors of sensory neurons in human nervous system, which can recognize noxious stimuli and send warning signals to the central neural system via afferent nerve to initiate motor responses (Figure 4A).^{5,40,41} Although diffusive memristors have demonstrated their potential in emulation of nociceptors and spiking neurons,^{2,5,22,41} there has not yet

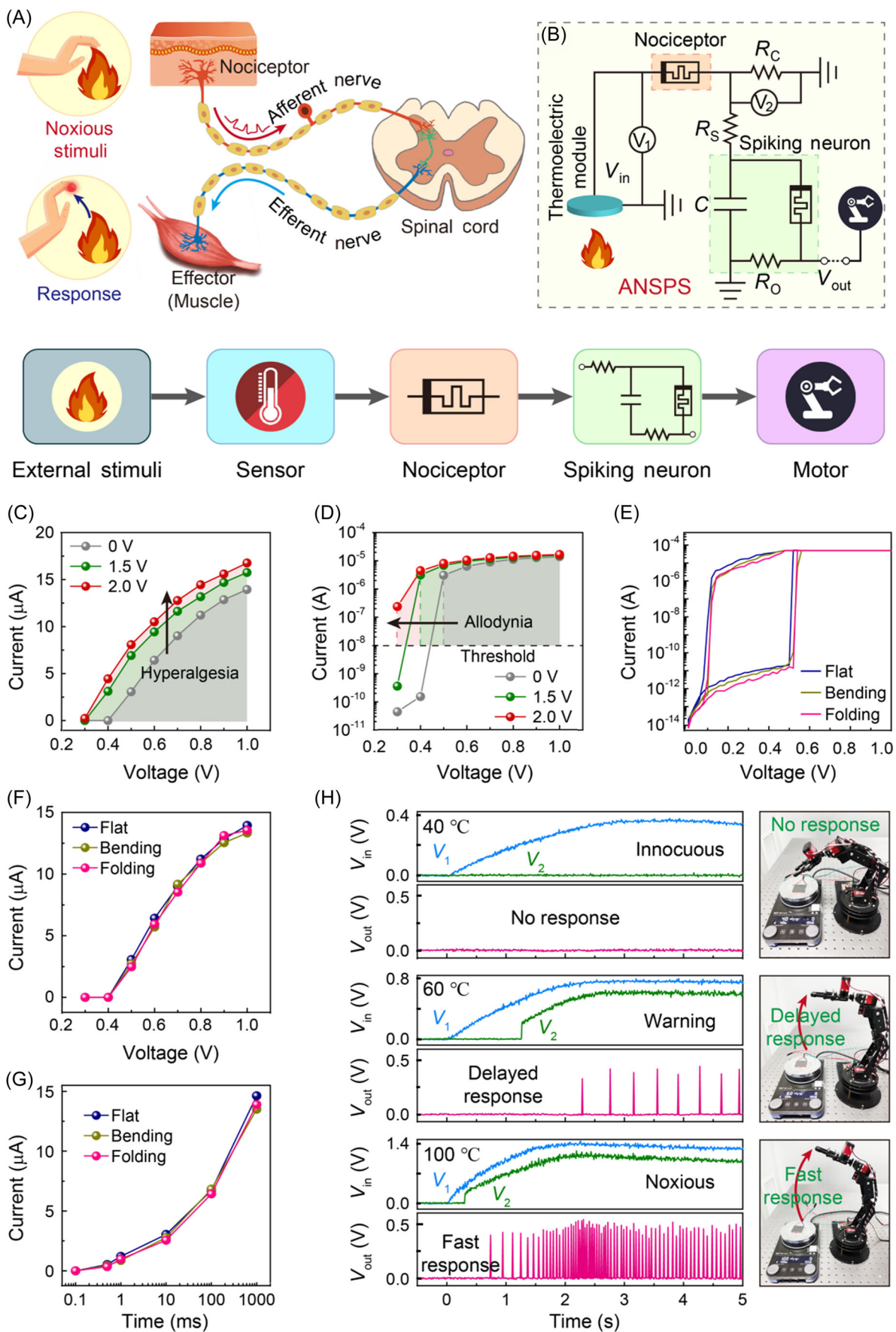


FIGURE 4 (See caption on next page)

been a demonstration of fully memristive ANSPS that integrates nociceptor and spiking neuron beyond CMOS techniques. Here a power-free ANSPS consisting of a sensor, a nociceptor, and a spiking neuron was developed (Figure 4B), in which both the nociceptor and spiking neuron were emulated by the CsPbBr₃@GDY-based memristors.^{42,43}

We first emulated the nociceptor using our memristor in TS mode. As discussed in Note S2, key features of biological nociceptors including “threshold,” “no-adaptation,” “relaxation,” and “sensitization” were successfully implemented by the TS-mode memristor. As shown in Figure S32, the output signals of the nociceptor are highly dependent on the intensity and width of the input stimuli, and the action potential (output current) is generated only when the input voltage exceeds the threshold (i.e., noxious stimulus). Figure S33 depicts the response of the artificial nociceptor triggered by trains of voltage pulses with different amplitudes. The output signals occur an abrupt increase after a certain number of stimuli, which is inversely proportional to the amplitude of the pulses. Once the device is turned on, it will sustain the current level without relaxation or degradation while applying extra number of pulses, which is similar to the “no adaptation” feature of a nociceptor. The “relaxation” characteristic is demonstrated in Figure S34, which exhibits an enhanced response for a second innocuous stimulus immediately following a first noxious stimulus. With the increase of the interval between the two stimuli, the intensity of the output signals decays, and the second innocuous stimulus cannot trigger the device while the interval exceeds the relaxation time of the nociceptor. Sensitization is an essential function to protect the injured area by enhancing the sensitivity of nociceptor to stimuli.^{5,40,41,44} As shown in Figure S35, the nociceptor was first injured by applying voltage pulses with amplitudes of 1.5 V and 2.0 V, respectively, and the output signals of the “injured” nociceptor triggered by different voltage pulses (0.3 V–1.0 V, 10 ms) were measured. The nociceptor features a reduced threshold voltage and enhanced output current in comparison

with that of an uninjured nociceptor (Figure 4C,D), demonstrating the “allodynia” and “hyperalgesia” characteristics of biological nociceptors. Moreover, the injured nociceptor can be healed passively or actively with time passing or by applying negative pulses (Figure S36), which is similar to the “cure” process of biological nociceptors. Hence, all the signatures of biological nociceptors can be comprehensively emulated by a single CsPbBr₃@GDY-based memristor, while it requires at least six transistors and one capacitor for the CMOS-based counterparts.^{5,40}

Flexibility is essential for the application of nociceptor in robotics and wearable electronics.^{45,46} Here the flexibility of the memristor and the performance of the nociceptor in the bending and folding states were investigated. Figure S37 depicts the *I*–*V* characteristics of the memristor in RS mode with different bending radii and bending cycles, respectively. The V_{SET} and V_{RESET} , as well as the HRS and LRS exhibit a relatively small variation during the bending test (Figure S38), demonstrating excellent flexibility of the memristor. Figure 4E–G compares the response of the nociceptor in the flat, bending and folding states, respectively. No noticeable performance degradation was observed during the bending test, demonstrating the potential of the nociceptor in flexible applications.

Here a LIF circuit^{7,18,22} based on a TS-mode memristor (Figure S39) was used as the spiking neuron to transform continuous current signals collected from the nociceptor into spikes. As discussed in Note S3, the frequency of the output spikes is in proportion to the intensity of the input current (Figure S40), and thus the spiking neuron can serve as a current-to-frequency converter and encode noxious stimulus intensity to output firing rate. As a demonstration of our ANSPS, we demonstrated real-time detection and processing of noxious hot stimuli to drive the escape of a robotic arm. Here a thermoelectric module was used to detect external stimuli and convert them to voltage signals as input (Figure S41). When the voltage exceeded the threshold of the nociceptor (i.e., noxious stimulus), a high output response was generated and relayed to the spiking neuron. The spiking signals generated by the spiking

FIGURE 4 Power-free ANSPS for robotics. (A) Schematic of nociceptive signal processing in biological nervous system. (B) Illustration of the ANSPS consisting a sensor, a nociceptor and a spiking neuron. (C and D) The maximum output currents of the memristor at different injured states as a function of input voltage amplitudes in (C) linear and (D) logarithmic scale, respectively, demonstrating the enhanced output currents (hyperalgesia) and reduced threshold voltages (allodynia). (E) *I*–*V* curves of the TS-mode memristor in the flat, bending, and folding states, respectively. (F and G) Response intensity of the nociceptor triggered by voltage stimuli with different (F) intensities and (G) widths, respectively. The data were extracted from Figure S32. (H) Response of the ANSPS to innocuous stimulation (40°C, upper panel), warning stimulation (60°C, middle panel), and noxious stimulation (100°C, lower panel), respectively. V_1 and V_2 represent the voltage measured at positions as marked in (B). ANSPS, artificial nociceptive signal processing system.

neuron were then sent to the motor controller to drive the escape of robotic arm from the hot source. Figure 4H presents the response of the ANSPS to different temperature stimulation. For temperatures below 40°C, which was innocuous to the nociceptor, the ANSPS did not generate any output signals, and thus there was no motion for the robotic arm. For a higher temperature, e.g., 60°C, it can be regarded as a warning stimulation to the nociceptor since prolonged stimulation will induce an injury. In this case, spikes were generated with a few seconds delay, and the robotic arm escaped from the hot source after receiving the spiking signals. For an extremely high temperature (100°C), it produced an intense voltage shock to the ANSPS, which can fire the spiking neuron and trigger the escape response of the robotic arm in a short time. These temperature-dependent responses of the ANSPS are similar to those of human. Our ANSPS provides a feasible and simple solution with minimal hardware for sensory signal processing in humanoid robot.

2.5 | Spiking neural networks for unsupervised learning

As the third-generation ANN, SNN consisting of artificial synapses and spiking neurons shares large similarity with biological nervous systems and provides a time- and energy-efficient way to implement neuromorphic computing.^{18,22,47} The crossbar structure of memristor arrays provides a simple and efficient approach to construct hardware SNNs. Recently, LIF neurons based on diffusive memristors have been demonstrated,^{18,22} making it possible to develop fully memristive SNNs. Here we demonstrate the first fully memristive SNN based on homo-material memristor arrays, in which the RS-mode and TS-mode of our dual-mode memristors (RSM/TSM) serve as artificial synapses and output neurons, respectively. Figure 5A,B illustrates the schematic of a two-layer SNN, which consists of 30 input neurons, 300 synapses, and 10 output neurons. As an exemplification, unsupervised learning for digit recognition has been

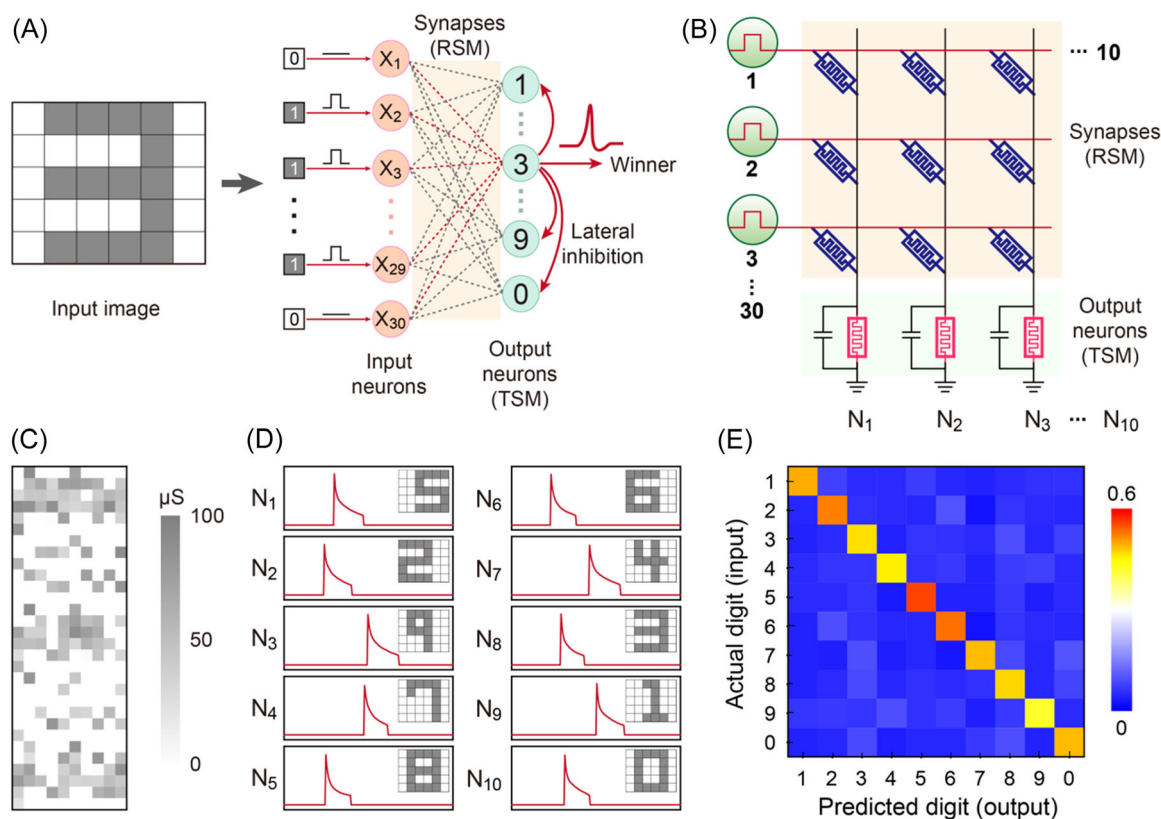


FIGURE 5 Fully memristive SNN for pattern classification. (A) Schematic of the two-layer SNN consisting of RSM synapses and TSM output neurons for digit recognition. (B) Illustration of the fully memristive SNN based on dual-mode memristor arrays in RS and TS modes for synapses and output neurons, respectively. (C) Conductance map of the RSM array after training. (D) Simulated output signals of the fired output neurons for the corresponding digits. N_1 – N_{10} represent the 10 output neurons as illustrated in (B). (E) Confusion matrix between actual (input) and predicted (output) digits. Large values along the diagonal line demonstrate the successful recognition of digits by the fully memristive SNN. RSM, RS-mode; SNN, spiking neural network.

performed by this SNN. Figure S42 presents the images of 0–9 with 5×6 pixels,^{20,22} for which the black and white squares correspond to an input voltage pulse of 1 V and 0 V, respectively. These images are flattened into one-dimensional (1D) vectors, and each pixel is mapped to one input neuron. The TSM-based output neurons are fully connected to the input neurons by the RSM-based synapses. Lateral inhibitory paths are added to the output neurons for Winner-Take-All fashion.^{18,22}

A training process was first carried out to build strong correlation between the input images and output neurons.²⁰ Before training, all the RSM-based synapses were initialized to HRS with some stochastic variation (Figure S43). The SNN was trained off-line and the corresponding weight values after training were written into the RSM array, just as shown in Figure 5C. It is worth noting that each output neuron fires just once during the training process. After training, the SNN was tested with the digit images. For example, an input image of “3” was mapped to the 30 input nodes, and the 10 output neurons integrated the current across the memristor array. Due to the strong correlation between the input maps and the trained memristors, the output neuron that was trained for “3” fired first, and the other neurons were inhibited by the Winner-Take-All rule.^{18,22} Figures 5D and S44 depict the simulated output signals of the 10 output neurons for the corresponding input digit images, in which only the associated output neuron fires while the other neurons remain at 0. The output currents of the 10 output neurons for digits of 0–9 are extracted and mapped in Figure 5E, presenting a diagonal matrix with one-to-one correspondence as expected. The successful recognition of digit images demonstrates the great potential of our dual-mode memristors in hardware SNNs for neuromorphic computing.

3 | CONCLUSION

In summary, we have proposed a flexible dual-mode memristor array based on core-shell CsPbBr₃@GDY nanocrystals, which features optically modulated RS and TS behaviors with a transition yield of 100%. On the basis of this memristor, a power-free ANSPS consisting of a thermoelectric module, a nociceptor, and a spiking neuron is developed, which can perceive external continuous stimulation and output spiking signals just like human nervous system, providing a feasible and simple solution with minimal hardware for sensory signal processing in humanoid robot. Moreover, a fully memristive SNN is constructed, in which both the synapses and output neurons are implemented by the CsPbBr₃@GDY-based dual-mode memristors. To the best of our knowledge, this is the first homo-

material-based fully memristive SNN. Compared with other MHP-based neuromorphic devices, our memristor exhibits excellent environmental stability due to the encapsulation of the shell GDY layer, making it possible for practical applications. This dual-mode memristor paves a simple way to construct fully memristive neuromorphic computing hardware at the system level.

ACKNOWLEDGMENTS

This study was supported by the National Natural Science Foundation of China (Nos. 21790052, 51802220) and the Natural Science Foundation of Tianjin City (No. 19JCYBJC17300).

CONFLICTS OF INTEREST

The authors declare no conflicts of interest.

DATA AVAILABILITY STATEMENT

The data that supports the findings of this study are available in the supplementary material of this article.

ORCID

Xu-Dong Chen  <https://orcid.org/0000-0002-0184-3953>

REFERENCES

- Xia Q, Yang JJ. Memristive crossbar arrays for brain-inspired computing. *Nat Mater.* 2019;18(4):309-323.
- Zhang X, Zhuo Y, Luo Q, et al. An artificial spiking afferent nerve based on Mott memristors for neurorobotics. *Nat Commun.* 2020;11:51.
- Gao S, Yi X, Shang J, Liu G, Li R-W. Organic and hybrid resistive switching materials and devices. *Chem Soc Rev.* 2019;48(6):1531-1565.
- Yao B-W, Li J, Chen X-D, et al. Non-volatile electrolyte-gated transistors based on graphdiyne/MoS₂ with robust stability for low-power neuromorphic computing and logic-in-memory. *Adv Funct Mater.* 2021;31(25):2100069.
- John RA, Yantara N, Ng SE, et al. Diffusive and drift halide perovskite memristive barristors as nociceptive and synaptic emulators for neuromorphic computing. *Adv Mater.* 2021; 33(15):2007851.
- Hou Y-X, Li Y, Zhang Z-C, et al. Large-scale and flexible optical synapses for neuromorphic computing and integrated visible information sensing memory processing. *ACS Nano.* 2021;15(1):1497-1508.
- Wang J, Lv Z, Xing X, et al. Optically modulated threshold switching in core-shell quantum dot based memristive device. *Adv Funct Mater.* 2020;30(16):1909114.
- Zhang B, Chen W, Zeng J, et al. 90% yield production of polymer nano-memristor for in-memory computing. *Nat Commun.* 2021;12:1984.
- Zhang Z-C, Li Y, Li J, et al. An ultrafast nonvolatile memory with low operation voltage for high-speed and low-power applications. *Adv Funct Mater.* 2021;31:2102571.
- Zhang Z-C, Li Y, Wang J-J, et al. Synthesis of wafer-scale graphdiyne/graphene heterostructure for scalable neuromorphic

- computing and artificial visual systems. *Nano Res.* 2021;14:4591-4600.
11. Sangwan VK, Hersam MC. Neuromorphic nanoelectronic materials. *Nat Nanotechnol.* 2020;15(7):517-528.
 12. Seo S, Jo S-H, Kim S, et al. Artificial optic-neural synapse for colored and color-mixed pattern recognition. *Nat Commun.* 2018;9:5106.
 13. Gao J, Zheng Y, Yu W, et al. Intrinsic polarization coupling in 2D α -In₂Se₃ toward artificial synapse with multimode operations. *SmartMat.* 2021;2(1):88-98.
 14. Li C, Hu M, Li Y, et al. Analogue signal and image processing with large memristor crossbars. *Nat Electron.* 2018;1(1):52-59.
 15. Prezioso M, Merrih-Kh-Bayat F, Hoskins BD, Adam GC, Likharev KK, Strukov DB. Training and operation of an integrated neuromorphic network based on metal-oxide memristors. *Nature.* 2015;521(7550):61-64.
 16. Yang F, Sun L, Duan Q, et al. Vertical-organic-nanocrystal-arrays for crossbar memristors with tuning switching dynamics toward neuromorphic computing. *SmartMat.* 2021;2(1):99-108.
 17. Li Y, Qian Q, Zhu X, et al. Recent advances in organic-based materials for resistive memory applications. *InfoMat.* 2020;2(6):995-1033.
 18. Wang Z, Joshi S, Savel'ev S, et al. Fully memristive neural networks for pattern classification with unsupervised learning. *Nat Electron.* 2018;1(2):137-145.
 19. Pei Y, Yan L, Wu Z, et al. Artificial visual perception nervous system based on low-dimensional material photoelectric memristors. *ACS Nano.* 2021;15(11):17319-17326.
 20. Chu M, Kim B, Park S, et al. Neuromorphic hardware system for visual pattern recognition with memristor array and CMOS neuron. *IEEE T Ind Electron.* 2015;62(4):2410-2419.
 21. Mahowald M, Douglas R. A silicon neuron. *Nature.* 1991;354(6354):515-518.
 22. Zhang X, Wang W, Liu Q, et al. An artificial neuron based on a threshold switching memristor. *IEEE Electr Device L.* 2018;39(2):308-311.
 23. Wang H, Du Y, Li Y, et al. Configurable resistive switching between memory and threshold characteristics for protein-based devices. *Adv Funct Mater.* 2015;25(25):3825-3831.
 24. Lin C-Y, Chen P-H, Chang T-C, et al. Attaining resistive switching characteristics and selector properties by varying forming polarities in a single HfO₂-based RRAM device with a vanadium electrode. *Nanoscale.* 2017;9(25):8586-8590.
 25. Jeong B, Gkoupidenis P, Asadi K. Solution-processed perovskite field-effect transistor artificial synapses. *Adv Mater.* 2021;33(52):2104034.
 26. Wang Y, Lv Z, Liao Q, et al. Synergies of electrochemical metallization and valence change in all-inorganic perovskite quantum dots for resistive switching. *Adv Mater.* 2018;30(28):1800327.
 27. Liu Y, Dong B, Hagfeldt A, Luo J, Graetzel M. Chemically tailored molecular surface modifiers for efficient and stable perovskite photovoltaics. *SmartMat.* 2021;2(1):33-37.
 28. Yang L, Singh M, Shen SW, et al. Transparent and flexible inorganic perovskite photonic artificial synapses with dual-mode operation. *Adv Funct Mater.* 2021;31(6):2008259.
 29. Xiao X, Hu J, Tang S, et al. Recent advances in halide perovskite memristors: materials, structures, mechanisms, and applications. *Adv Mater Technol.* 2020;5(6):1900914.
 30. Zhang C, Li Y, Ma C, Zhang Q. Recent progress of organic-inorganic hybrid perovskites in RRAM, artificial synapse, and logic operation. *Small Sci.* 2022;2(2):2100086-2100561.
 31. Wei Y, Cheng Z, Lin J. An overview on enhancing the stability of lead halide perovskite quantum dots and their applications in phosphor-converted leds. *Chem Soc Rev.* 2019;48(1):310-350.
 32. Cho H, Kim Y-H, Wolf C, Lee H-D, Lee T-W. Improving the stability of metal halide perovskite materials and light-emitting diodes. *Adv Mater.* 2018;30(42):1704587.
 33. Yin C, Li J, Li T, et al. Catalyst-free synthesis of few-layer graphdiyne using a microwave-induced temperature gradient at a solid/liquid interface. *Adv Funct Mater.* 2020;30(23):2001396.
 34. Li G, Li Y, Liu H, Guo Y, Li Y, Zhu D. Architecture of graphdiyne nanoscale films. *Chem Commun.* 2010;46(19):3256-3258.
 35. Li J, Zhang Z, Kong Y, et al. Synthesis of wafer-scale ultrathin graphdiyne for flexible optoelectronic memory with over 256 storage levels. *Chem.* 2021;7(5):1284-1296.
 36. Wu H, Kang Z, Zhang Z, et al. Interfacial charge behavior modulation in perovskite quantum dot-monolayer MoS₂ 0D-2D mixed-dimensional van der waals heterostructures. *Adv Funct Mater.* 2018;28(34):1802015.
 37. Chen S, Mahmoodi MR, Shi Y, et al. Wafer-scale integration of two-dimensional materials in high-density memristive crossbar arrays for artificial neural networks. *Nat Electron.* 2020;3(10):638-645.
 38. Ji W, Zhou H, Ye Y, et al. Trap-related nonvolatile negative photoconductivity in a single Ag@Al₂O₃ hybrid nanorod for a photomemory with light-writing and bias-erasing. *Adv Opt Mater.* 2019;7(24):1901154.
 39. Wang X-H, Zhang Z-C, Wang J-J, et al. Synthesis of wafer-scale monolayer pyrenyl graphdiyne on ultrathin hexagonal boron nitride for multibit optoelectronic memory. *ACS Appl Mater Interfaces.* 2020;12(29):33069-33075.
 40. John RA, Tiwari N, Patdillah MIB, et al. Self healable neuromorphic memtransistor elements for decentralized sensory signal processing in robotics. *Nat Commun.* 2020;11:4030.
 41. Yoon JH, Wang Z, Kim KM, et al. An artificial nociceptor based on a diffusive memristor. *Nat Commun.* 2018;9:417.
 42. Chen Y, Gao Z, Zhang F, Wen Z, Sun X. Recent progress in self-powered multifunctional e-skin for advanced applications. *Exploration.* 2022;2(1):20210112.
 43. Zhang Y, Gao X, Wu Y, et al. Self-powered technology based on nanogenerators for biomedical applications. *Exploration.* 2021;1(1):90-114.
 44. Deng X, Wang SQ, Liu YX, et al. A flexible mott synaptic transistor for nociceptor simulation and neuromorphic computing. *Adv Funct Mater.* 2021;31(23):2101099.
 45. Zhou K, Dai K, Liu C, Shen C. Flexible conductive polymer composites for smart wearable strain sensors. *SmartMat.* 2020;1(1):e1010.
 46. Li Y, Zhang C, Shi Z, Ma C, Wang J, Zhang Q. Recent advances on crystalline materials-based flexible memristors for data storage and neuromorphic applications. *Sci China Mater.* 2021;65:2110-2127.

47. Li Y, Lu J, Shang D, et al. Oxide-based electrolyte-gated transistors for spatiotemporal information processing. *Adv Mater.* 2020;32(47):2003018.

SUPPORTING INFORMATION

Additional supporting information can be found online in the Supporting Information section at the end of this article.

How to cite this article: Wang F-D, Yu M-X, Chen X-D, et al. Optically modulated dual-mode memristor arrays based on core-shell CsPbBr₃@graphdiyne nanocrystals for fully memristive neuromorphic computing hardware. *SmartMat.* 2023;4:e1135. doi:10.1002/smm2.1135